Monthly Notices of the ROYAL ASTRONOMICAL SOCIETY

MNRAS **500,** 986–997 (2021) doi:10.1093/mnras/staa3297
Advance Access publication 2020 October 27

Search for globular clusters associated with the Milky Way dwarf galaxies using *Gaia* DR2

Kuan-Wei Huang [1]★ and Sergey E. Koposov [1,2,3]

[1] *McWilliams Center for Cosmology, Department of Physics, Carnegie Mellon University, Pittsburgh, PA 15213, USA*
[2] *Institute for Astronomy, University of Edinburgh, Royal Observatory, Blackford Hill, Edinburgh EH9 3HJ, UK*
[3] *Institute of Astronomy, Madingley Rd, Cambridge CB3 0HA, UK*

Accepted 2020 October 20. Received 2020 October 19; in original form 2020 May 28

ABSTRACT

We report the result of searching for globular clusters (GCs) around 55 Milky Way (MW) satellite dwarf galaxies within the distance of 450 kpc from the Galactic Centre except for the Large and Small Magellanic Clouds and the Sagittarius dwarf. For each dwarf, we analyse the stellar distribution of sources in *Gaia* DR2, selected by magnitude, proper motion, and source morphology. Using the kernel density estimation of stellar number counts, we identify 11 possible GC candidates. Cross-matched with existing imaging data, all 11 objects are known either GCs or galaxies and only Fornax GC 1–6 among them are associated with the targeted dwarf galaxy. Using simulated GCs, we calculate the GC detection limit $M_{\rm V}^{\rm lim}$ that spans the range from $M_{\rm V}^{\rm lim} \sim -7$ for distant dwarfs to $M_{\rm V}^{\rm lim} \sim 0$ for nearby systems. Assuming a Gaussian GC luminosity function, we compute that the completeness of the GC search is above 90 per cent for most dwarf galaxies. We construct the 90 per cent credible intervals/upper limits on the GC specific frequency $S_{\rm N}$ of the MW dwarf galaxies: $12 < S_{\rm N} < 47$ for Fornax, $S_{\rm N} < 20$ for the dwarfs with $-12 < M_{\rm V} < -10$, $S_{\rm N} < 30$ for the dwarfs with $-10 < M_{\rm V} < -7$, and $S_{\rm N} < 90$ for the dwarfs with $M_{\rm V} > -7$. Based on $S_{\rm N}$, we derive the probability of galaxies hosting GCs given their luminosity, finding that the probability of galaxies fainter than $M_{\rm V} = -9$ to host GCs is lower than 0.1.

Key words: globular clusters: general – galaxies: dwarf.

1 INTRODUCTION

Globular clusters (GCs) are some of the oldest luminous observable objects with ages comparable to the age of the Universe (VandenBerg et al. 2013). Characterized by being compact and bright, GCs typically have masses of 10^4–10^6 $M_\odot$, luminosities of $M_{\rm V} = -5$ to -10, and sizes of a few parsecs (Harris 1991; Brodie & Strader 2006). GCs might have played an important role in the early formation of galaxies, and they could have been the potential drivers of cosmic reionization (Boylan-Kolchin 2018) despite the issues with the escape fraction of ionizing radiation (Howard et al. 2018b; He, Ricotti & Geen 2020). However, the formation of GCs themselves remains an open question in astrophysics (some recent literature that discuss the formation of GCs, e.g. Howard, Pudritz & Harris 2018a; Choksi & Gnedin 2019; El-Badry et al. 2019; Reina-Campos et al. 2019; Ma et al. 2020). For detailed reviews of GCs, we refer readers to Gratton, Sneden & Carretta (2004), Brodie & Strader (2006), and Gratton et al. (2019).

In the Milky Way (MW), the number of known GCs has increased to around 150 (Harris 1996, 2010) since the first one was discovered in 1665 by Abraham Ihle. While some of these GCs that are more concentrated around the Galactic Centre are believed to have been formed *in situ* (Forbes, Brodie & Grillmair 1997; Harris, Harris & Poole 1999), the ones in the outskirts are believed to have been accreted together with their parent dwarf galaxies (e.g. Searle & Zinn 1978; Mackey & Gilmore 2004; Beasley et al. 2018; Kruijssen et al. 2019), which were destroyed by tides. Some of the GCs however can still be found within the MW satellites themselves, offering a window on the formation of GCs in dwarf galaxies. The three most luminous MW satellites, the Large and Small Magellanic Clouds (LMC and SMC) and the Sagittarius dwarf spheroidal galaxy, have large populations of GCs (Mackey & Gilmore 2003a, b, c; McLaughlin & van der Marel 2005). In particular, the clusters of the Sagittarius dwarf are spread out along the stellar stream (Lynden-Bell & Lynden-Bell 1995; Bellazzini, Ferraro & Ibata 2003; Luque et al. 2017; Vasiliev 2019), and the SMC has a large population of star clusters in general but few of them are classically old GCs. The only other two MW satellite galaxies known to possess GCs are the Fornax dwarf spheroidal galaxy that is the fourth most luminous MW satellite with six GCs, and the Eridanus 2, an ultra-faint system containing a faint cluster (Koposov et al. 2015; Crnojević et al. 2016).

The fact that some GCs in the MW still have been found until recently (Koposov et al. 2015; Koposov, Belokurov & Torrealba 2017; Wang et al. 2019) motivates us to further search for possibly missing ones. Intuitively, faint GCs within dwarf galaxies are more likely to have been missed, especially when located within luminous dwarf galaxies where the ground-based data can be crowded e.g. Fornax 6. Instead of looking for this kind of objects by chance, we apply the systemic overdensity searching algorithm (which will be explained in Section 2) to the areas around the MW satellite galaxies within the distance of 450 kpc except for the three most luminous

★ E-mail: kuanweih@andrew.cmu.edu

ones: the LMC, the SMC, and the Sagittarius dwarf. That is, we target the areas where GCs are likely to lurk from previous inspections of deep imaging to look for overdensities in dense dwarfs.

Focusing on a small area of the sky, a targeted search is less computationally expensive so that it can afford a lower detection threshold. For each targeted area, we investigate the stellar distribution in the *Gaia* data to detect possible GC candidates (see Section 2.1 for more detail about *Gaia* and the data set). Thanks to the high angular resolution that exceeds most ground-based surveys, *Gaia* allows us to detect previously missed objects that are not well resolved or missed by ground-based searches. For instance, Koposov et al. (2017) has found star clusters in *Gaia* that were missed by previous searches.

We organize the paper as follows. In Section 2, we explain the methodology with more detail about the *Gaia* data, sample selection, and kernel density estimation procedure. In Section 3, we demonstrate the main results of the detection. In Section 4, we discuss the limit and completeness of the detection, the inferred specific frequency of GCs, and the derived probability of dwarfs to host GCs based on our findings. In Section 5, we conclude the paper.

2 METHODOLOGY

2.1 *Gaia* DR2 and data selection

The space-based astrometric mission *Gaia* was launched by the European Space Agency in 2013 and started the whole-sky survey in 2014 (Gaia Collaboration 2016). Released in 2018, the second *Gaia* data release (*Gaia* DR2) contains the data collected during the first 22 months of the mission (Gaia Collaboration 2018a) and has approximately 1.7 billion sources with 1.3 billion parallaxes and proper motions. *Gaia* DR2 therefore provides high-resolution stellar distribution in the MW for us to look for possibly missing GCs around the MW dwarf galaxies. The overall scientific validation of the data is described in Arenou et al. (2018).

The entire analysis of this paper utilizes the `GAIA_SOURCE` catalogue of *Gaia* DR2 (ESA & DPAC 2019), particularly the position `ra` and `dec` (α and δ), the proper motion (PM) `pmra` and `pmdec` (μ_α and μ_δ), the G-band magnitude `phot_g_mean_mag` (G), and the value of the `astrometric_excess_noise` parameter (ϵ). Gaia Collaboration (2018a) contains the detail on the contents and the properties of this catalogue. We use this data set to identify stellar density peaks as possible candidates of GCs around in the vicinity and inside nearby dwarf galaxies.

Throughout the whole paper, we apply two main selection cuts on the *Gaia* catalogue. The first selection is

$$17 < G < 21. \tag{1}$$

The faint-magnitude cut $G < 21$ approximately corresponds to the faint-end limit of *Gaia* DR2; Gaia Collaboration (2018a) reported that only 4 per cent of the sources are fainter than $G = 21$ and those sources lack PMs and parameters. There are two reasons for the bright-magnitude cut $G > 17$. The first reason to get rid of the bright stars is that the foreground contamination dominates at bright magnitudes. Conversely, the expected rapid rise of the stellar luminosity function for the majority of GCs and dwarf galaxies at reasonable distances from the Sun at $G > 17$ results in the majority of stars being fainter than $G = 17$. The other reason is that most bright GCs with large numbers of $G < 17$ stars would have likely been detected already. The second selection criterion is

$$\ln \epsilon < 1.5 + 0.3 \max\{G - 18, 0\}. \tag{2}$$

This cut is used to reject potentially extended sources (see Koposov et al. 2017; Wang et al. 2019, for more detail).

Another optional selection that we use to further clean the source list is based on the PM, with the goal of removing sources whose PMs are different from the mean PM of a given targeted dwarf galaxy, as these sources are less likely to be member stars of the given dwarf. For each targeted dwarf, we exclude stars with PMs (μ_α, μ_δ) differing from a systemic PM of the dwarf ($\mu_\alpha^{\rm dwarf}$, $\mu_\delta^{\rm dwarf}$) by more than three times the PM uncertainty (σ_{μ_α}, σ_{μ_δ}). That is, only the stars satisfying

$$\sqrt{\left(\mu_\alpha - \mu_\alpha^{\rm dwarf}\right)^2 + \left(\mu_\delta - \mu_\delta^{\rm dwarf}\right)^2} < 3\sqrt{\sigma_{\mu_\alpha}^2 + \sigma_{\mu_\delta}^2} \tag{3}$$

survive after the PM selection.

For example, Fig. 1 shows the *Gaia* sources around the Fornax dwarf before and after the PM selection in equation (3). The source distribution in PM space in the left-hand panel shows that there are many foreground sources with PMs that are 10–100 mas yr^{-1} different from the PM of the dwarf. This PM selection is thus applied to remove this kind of contamination; the sources coloured in orange survive after the selection. It is worth noting that the PM uncertainty of the studied dwarfs is around the order of 10^3–10^5 km s^{-1} (see Table 1) that is much larger than the typical velocity dispersion of dwarf galaxies around the order of 10 km s^{-1} (Walker et al. 2007) or 0.02 mas yr^{-1} if at 100 kpc, so the survived sources under this PM selection still have a fairly large range of internal space velocity. To investigate the PM selection for the stars that are more likely to be member stars of the Fornax dwarf, we draw a lasso with the black dashed lines to roughly distinguish the member stars in the red-giant branch of Fornax from the other stars in the colour–magnitude diagram in the right-hand panel. For the stars that are likely to be member stars inside of the lasso, 91 per cent of the sources survive after the PM selection, whereas most of the sources outside of the lasso are excluded. Moreover, in the left-hand panel of Fig. 2, the stellar distribution after the PM selection retains the shape of the Fornax dwarf.

2.2 Kernel density estimation

Convolving the spatial distribution of the data with various kernels is a common approach to identify the excess number of stars associated with a satellite or clusters in imaging data. The density is calculated by convolving all the data points interpreted as delta functions with different kernels, e.g. a moving average in Walsh, Willman & Jerjen (2009), two circular indicator functions in Torrealba, Belokurov & Koposov (2019a), and Gaussian kernels in Koposov, Glushkova & Zolotukhin (2008a), Koposov et al. (2008b), and Drlica-Wagner et al. (2015).

To identify star clusters in dwarf galaxies, we use the kernel density estimation on the stellar distribution, while assuming the Poisson distribution of stellar number counts.

(i) We obtain the distribution of stars

$$\Sigma(x, y) = \sum_i \delta(x - x_i, y - y_i), \tag{4}$$

where (x_i, y_i) is the position of the $i^{\rm th}$ star on the local coordinates that takes care of the projection effect.[1]

[1] In the algorithm, we always divide a targeted area into small patches with a side of 0.5°. For each patch centred at (α_0, δ_0), we define the local coordinates (x, y) with the origin of $(x_0, y_0) = (\alpha_0, \delta_0)$. Since the patch is very small, we approximate the projection effect as $x \approx (\alpha - \alpha_0)\cos\delta_0$ and $y = \delta - \delta_0$.

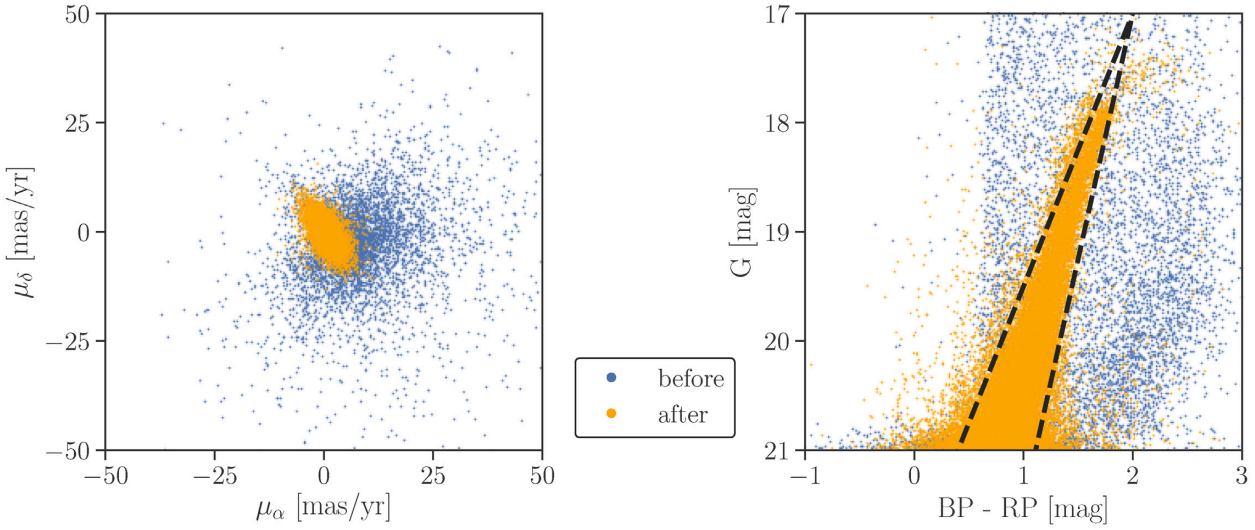

Figure 1. The *Gaia* sources around the Fornax dwarf before (blue) and after (orange) the proper motion selection defined in equation (3). *Left*: the distribution in proper motion space. *Right*: the colour–magnitude diagram. The black dashed lines define a lasso to roughly distinguish possible member stars in the red-giant branch of Fornax.

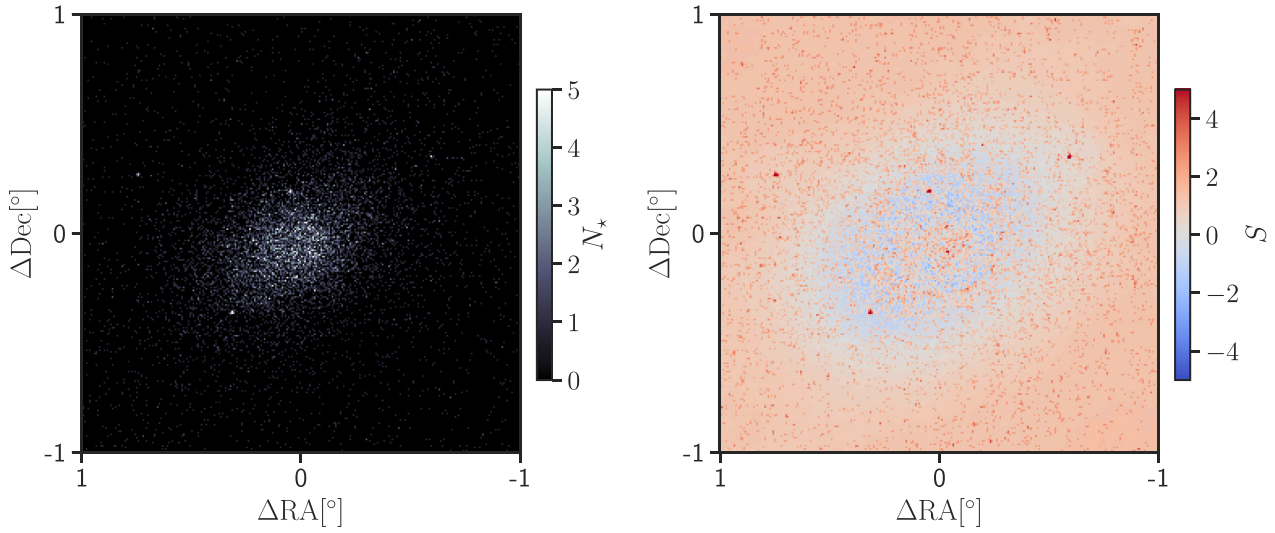

Figure 2. *Left*: the 2D histogram of *Gaia* DR2 sources selected using equations (1), (2), and (3) around the Fornax dwarf. *Right*: the overdensity significance (S) map according to equation (8).

(ii) Using the circular indicator function with a given radius R defined as $\mathbb{1}(x, y; R) = \begin{cases} 1 \text{ if } x^2 + y^2 \leq R^2 \\ 0 \text{ otherwise} \end{cases}$, we define the inner kernel $K_{\rm in}(x, y; \sigma_1) = \mathbb{1}(x, y; \sigma_1)$, where σ_1 corresponds to the scale of GCs which is 3, 5, or 10 pc. We then convolve $\Sigma(x, y)$ with $K_{\rm in}(x, y; \sigma_1)$ to estimate the number density of stars on the scale of σ_1 as

$$\Sigma_{\rm in}(x, y) = \Sigma(x, y) * K_{\rm in}(x, y; \sigma_1). \quad (5)$$

(iii) Defining the outer kernel $K_{\rm out}(x, y; \sigma_1, \sigma_2) = \mathbb{1}(x, y; \sigma_2) - \mathbb{1}(x, y; 2\sigma_1)$, we convolve $\Sigma(x, y)$ with $K_{\rm out}(x, y; \sigma_1, \sigma_2)$ as

$$\Sigma_{\rm out}(x, y) = \Sigma(x, y) * K_{\rm out}(x, y; \sigma_1, \sigma_2) \quad (6)$$

to estimate the number density of stars on the annular area of radius between $2\sigma_1$ and σ_2, where $\sigma_2 > 2\sigma_1$ and σ_2 correspond to either the angular scale of parent dwarf galaxy or a fixed angular scale of 0.5° (see more detail in the next paragraph).

(iv) We estimate the expected background number density within the inner kernel from $\Sigma_{\rm out}(x, y)$ through the ratio of the inner and outer areas

$$\Sigma_{\rm bg}(x, y) = \frac{\sigma_1^2}{\sigma_2^2 - (2\sigma_1)^2} \Sigma_{\rm out}(x, y). \quad (7)$$

(v) We convert the tail probability of Poisson into the z-score of the standard normal distribution to evaluate the significance as

$$S(x, y) = F^{-1}_{\rm N(0,1)} \left(F_{\rm Poi(\Sigma_{bg}(x,y))} \left(\Sigma_{\rm in}(x, y) \right) \right), \quad (8)$$

where F is the cumulative distribution function.

As an example, Fig. 2 shows the original 2D histogram of the sources around the Fornax dwarf in the left-hand panel and the significance map of that stellar distribution in the right-hand panel. According to the significance map, we identify positive detection

Table 1. The list of properties of the studied dwarf galaxies: the positions (α and δ), the heliocentric distance ($D_\odot$), the V-band magnitude (M_V), the proper motions (μ_α and μ_δ), the reference (ref.), and the 3 $\sigma_\mu = 3\sqrt{\sigma^2_{\mu_\alpha} + \sigma^2_{\mu_\delta}}$ PM uncertainty converted to km s^{-1} at the distance of the dwarf.

Dwarf	α [°]	δ [°]	$D_\odot$ [kpc]	M_V [mag]	ref.[a]	μ_α [mas yr^{-1}]	μ_δ [mas yr^{-1}]	ref.[a]	$3\sigma_\mu$ [km s^{-1}]
Antlia 2	143.89	− 36.77	132.0	− 9.0	T19b	− 0.095 ± 0.018	0.058 ± 0.024	T19b	2e+04
Aquarius 2	338.48	− 9.33	107.9	− 4.4	T16b	− 0.252 ± 0.526	0.011 ± 0.448	Fritz et al. (2018)	3e+05
Bootes I	210.02	14.50	66.4	− 6.3	M12	− 0.459 ± 0.041	− 1.064 ± 0.029	Gaia Collab. 18b.	2e+04
Bootes II	209.50	12.85	41.7	− 2.7	M12	− 2.686 ± 0.389	− 0.530 ± 0.287	Fritz et al. (2018)	9e+04
Bootes III	209.25	26.80	46.0	− 5.7	MH18	− 1.210 ± 0.130	− 0.920 ± 0.170	MH18	5e+04
Canes Venatici I	202.01	33.56	217.8	− 8.6	M12	− 0.159 ± 0.094	− 0.067 ± 0.054	Fritz et al. (2018)	1e+05
Canes Venatici II	194.29	34.32	100.0	− 4.9	M12	− 0.342 ± 0.232	− 0.473 ± 0.169	Fritz et al. (2018)	1e+05
Carina	100.40	− 50.97	105.2	− 9.1	M12	0.495 ± 0.015	0.143 ± 0.014	Gaia Collab. 18b.	1e+04
Carina 2	114.11	− 58.00	36.2	− 4.5	T18	1.810 ± 0.080	0.140 ± 0.080	MH18	2e+04
Carina 3	114.63	− 57.90	27.8	− 2.4	T18	3.035 ± 0.120	1.558 ± 0.136	Simon (2018)	2e+04
Cetus II	19.47	− 17.42	29.9	0.0	M12				
Cetus III	31.33	− 4.27	251.0	− 2.4	Homma18				
Columba I	82.86	− 28.03	182.0	− 4.5	M12	− 0.020 ± 0.240	− 0.040 ± 0.300	Pace & Li (2019)	3e+05
Coma Berenices	186.75	23.90	43.7	− 4.1	M12	0.471 ± 0.108	− 1.716 ± 0.104	Fritz et al. (2018)	3e+04
Crater 2	177.31	− 18.41	117.5	− 8.2	T16a	− 0.184 ± 0.061	− 0.106 ± 0.031	Fritz et al. (2018)	4e+04
Draco	260.05	57.92	75.9	− 8.8	M12	− 0.019 ± 0.009	− 0.145 ± 0.010	Gaia Collab. 18b.	5e+03
Draco II	238.20	64.57	24.0	− 2.9	M12	1.170 ± 0.297	0.871 ± 0.303	Simon (2018)	5e+04
Eridanus 2	56.09	− 43.53	380.2	− 6.6	M12	0.160 ± 0.240	0.150 ± 0.260	Pace & Li (2019)	6e+05
Eridanus 3	35.69	− 52.28	87.1	− 2.0	M12				
Fornax	40.00	− 34.45	147.2	− 13.4	M12	0.376 ± 0.003	− 0.413 ± 0.003	Gaia Collab. 18b.	3e+03
Grus I	344.18	− 50.16	120.2	− 3.4	M12	− 0.250 ± 0.160	− 0.470 ± 0.230	Pace & Li (2019)	2e+05
Grus II	331.02	− 46.44	53.0	− 3.9	M12	0.430 ± 0.090	− 1.450 ± 0.110	Pace & Li (2019)	3e+04
Hercules	247.76	12.79	131.8	− 6.6	M12	− 0.297 ± 0.118	− 0.329 ± 0.094	Fritz et al. (2018)	9e+04
Horologium I	43.88	− 54.12	79.4	− 3.4	M12	0.950 ± 0.070	− 0.550 ± 0.060	Pace & Li (2019)	3e+04
Horologium II	49.13	− 50.02	78.0	− 2.6	M12				
Hydra II	185.43	− 31.99	134.3	− 4.8	M12	− 0.416 ± 0.519	0.134 ± 0.422	Fritz et al. (2018)	4e+05
Indus I	317.20	− 51.17	100.0	− 3.5	M12				
Indus II	309.72	− 46.16	213.8	− 4.3	M12				
Leo I	152.12	12.31	253.5	− 12.0	M12	− 0.097 ± 0.056	− 0.091 ± 0.047	Gaia Collab. 18b.	9e+04
Leo II	168.37	22.15	233.4	− 9.8	M12	− 0.064 ± 0.057	− 0.210 ± 0.054	Gaia Collab. 18b.	8e+04
Leo IV	173.24	− 0.53	154.2	− 5.8	M12	− 0.590 ± 0.531	− 0.449 ± 0.358	Fritz et al. (2018)	5e+05
Leo V	172.79	2.22	177.8	− 5.3	M12	− 0.097 ± 0.557	− 0.628 ± 0.302	Fritz et al. (2018)	5e+05
Leo T	143.72	17.05	416.9	− 8.0	M12				
Pegasus 3	336.09	5.42	205.1	− 4.1	M12				
Phoenix	27.78	− 44.44	415.0	− 9.9	M12	0.079 ± 0.099	− 0.049 ± 0.120	Fritz et al. (2018)	3e+05
Phoenix 2	355.00	− 54.41	83.2	− 2.8	M12	0.490 ± 0.110	− 1.030 ± 0.120	Pace & Li (2019)	6e+04
Pictoris I	70.95	− 50.28	114.8	− 3.1	M12				
Pisces II	344.63	5.95	182.0	− 5.0	M12	− 0.108 ± 0.645	− 0.586 ± 0.498	Fritz et al. (2018)	7e+05
Reticulum II	53.93	− 54.05	30.2	− 2.7	M12	2.340 ± 0.120	− 1.310 ± 0.130	MH18	2e+04
Reticulum III	56.36	− 60.45	91.6	− 3.3	M12	− 1.020 ± 0.320	− 1.230 ± 0.400	Pace & Li (2019)	2e+05
Sagittarius II	298.17	− 22.07	67.0	− 5.2	M12	− 1.180 ± 0.140	− 1.140 ± 0.110	MH18	6e+04
Sculptor	15.04	− 33.71	85.9	− 11.1	M12	0.082 ± 0.005	− 0.131 ± 0.004	Gaia Collab. 18b.	3e+03
Segue I	151.77	16.08	22.9	− 1.5	M12	− 1.697 ± 0.195	− 3.501 ± 0.175	Fritz et al. (2018)	3e+04
Segue II	34.82	20.18	34.7	− 2.5	M12	1.270 ± 0.110	− 0.100 ± 0.150	MH18	3e+04
Sextans I	153.26	− 1.61	85.9	− 9.3	M12	− 0.496 ± 0.025	0.077 ± 0.020	Gaia Collab. 18b.	1e+04
Triangulum II	33.32	36.18	30.2	− 1.8	M12	0.651 ± 0.193	0.592 ± 0.164	Simon (2018)	4e+04
Tucana II	342.98	− 58.57	57.5	− 3.8	M12	0.910 ± 0.060	− 1.160 ± 0.080	Pace & Li (2019)	3e+04
Tucana III	359.15	− 59.60	25.2	− 2.4	M12	− 0.030 ± 0.040	− 1.650 ± 0.040	Pace & Li (2019)	7e+03
Tucana IV	0.73	− 60.85	48.1	− 3.5	M12	0.630 ± 0.250	− 1.710 ± 0.200	Pace & Li (2019)	7e+04
Tucana V	354.35	− 63.27	55.2	− 1.6	M12				
Ursa Major I	158.72	51.92	96.8	− 5.5	M12	− 0.659 ± 0.093	− 0.635 ± 0.131	Simon (2018)	7e+04
Ursa Major II	132.88	63.13	31.6	− 4.2	M12	1.661 ± 0.053	− 1.870 ± 0.065	Simon (2018)	1e+04
Ursa Minor	227.29	67.22	75.9	− 8.8	M12	− 0.182 ± 0.010	0.074 ± 0.008	Gaia Collab. 18b.	4e+03
Virgo I	180.04	− 0.68	87.0	− 0.8	Homma16				
Willman I	162.34	51.05	38.0	− 2.7	M12	0.199 ± 0.187	− 1.342 ± 0.366	Fritz et al. (2018)	7e+04

[a] Some of the citations are abbreviated: Gaia Collab. 18b. is for Gaia Collaboration (2018b); MH18 is for Massari & Helmi (2018); M12 is for McConnachie (2012); T18 is for Torrealba et al. (2018); T19b is for Torrealba et al. (2019b); T16b is for Torrealba et al. (2016b); T16a is for Torrealba et al. (2016a); Homma18 is for Homma et al. (2018); Hargis16 is for Hargis et al. (2016); and Homma16 is for Homma et al. (2016).

with significance higher than a certain significance threshold. For nearby pixels with significance higher than the threshold, we merge them as one single positive detection if the radial distance between the pixels is shorter than the size of the inner kernel. We assign the maximum significance on the merged pixels as the detected significance and use the centre of mass coordinates of the merged pixels as the detected position.

The main reason for σ_2 in step (iii) corresponding to either the angular scale of parent dwarf galaxy or the fixed angular scale of 0.5° is that the kernel density estimates are biased in crowded areas, which may lead to missing objects around big dwarfs. Given a dwarf with a half-light radius of r_h, σ_2 is chosen to be $0.5r_h$ or 0.5° for pixels inside ($r < r_h$) or outside ($r > r_h$) of the dwarf respectively, where r is the distance from the position of any pixel to the centre of the dwarf. The latter large σ_2 of 0.5° is to take care of the sparse outskirts of the dwarf. Besides, when dealing with the pixels outside of the dwarf, we exclude the effect of the pixels inside of the dwarf ($r_h < r < r_h + 0.5^\circ$) because the relatively high number density of stars in the dwarf will lead to overestimate of $\Sigma_{out}(x, y)$ that will suppress the background estimate too much later.

3 RESULTS

The objective of the paper is to search for possibly missing GCs around the MW satellites by identifying stellar overdensities with the searching algorithm described in Section 2.2. The list of dwarf galaxies considered in this paper was created by selecting dwarf galaxies within the distance of 450 kpc from the Galactic Centre with the exception of the LMC, the SMC, and the Sagittarius dwarf. The dwarf list in Table 1 summarizes all 55 targeted dwarfs investigated in the paper and their properties. The reason to exclude the three most massive satellites of the MW is that their relatively large sizes will lead to a huge portion of the sky to be searched, which conflicts with our goal of conducting a targeted search. In the construction of the dwarf galaxy list, we use the data from the McConnachie (2012) compilation and include some of the recent discoveries: Antlia 2 (Torrealba et al. 2019b), Aquarius 2 (Torrealba et al. 2016b), Bootes 3 (Massari & Helmi 2018), Carina 2 (Torrealba et al. 2018), Carina 3 (Torrealba et al. 2018), Cetus 3 (Homma et al. 2018), Crater 2 (Torrealba et al. 2016a), and Virgo I (Homma et al. 2016).

For each targeted dwarf, we search the area within the radius of $\min\{8^\circ, R_{vir}\}$, where R_{vir} is the virial radius of a 10^9 $M_\odot$ halo (Walker et al. 2007) (at the distance of 100 kpc this corresponds to 10°). We choose the inner kernel sizes of $\sigma_1 = 3$, 5, and 10 pc that covers the range of physical sizes of a typical GC (Brodie & Strader 2006). We run the searching algorithm for each inner kernel size on the *Gaia* sources after the selections of equation (3) if the dwarf has known measured PM (see Table 1), equations (1) and (2).

To balance the completeness of search with the number of false positives, we define two thresholds for identifying possible candidates: a significance threshold $S > 5$ and the limit of the number of stars inside the inner kernel $\Sigma_{in} > 10$. For $S > 5$, as the z-score of the standard normal distribution, its false alarm probability is of the order of 10^{-7}.[2] Assuming a targeted dwarf at the distance of 100 kpc with a searching radius of 8°, the total number of spatial pixels is around the order of 10^8.[3] With the false alarm probability $\sim 10^{-7}$ on the targeted area of $\sim 10^8$ pixels, the number of expected false positives is around the order of 10. Moreover, we apply the other threshold, $\Sigma_{in} > 10$, to prevent a large number of false positives for the pixels with very low background number density. For example, in Fig. 2, it is noticeable that the significance can easily be large in the area with very sparse stellar density even if only a handful of stars are detected in the inner kernel. These pixels typically have $\Sigma_{out} < 1$ where the significance estimator breaks down due to the very low rate parameter of Poisson. Hence by applying $\Sigma_{in} > 10$, we effectively increase the threshold on S for pixels with $\Sigma_{out} < 1$, e.g. the threshold is $S = 5.6$ for $\Sigma_{out} = 1$ and $S = 8.9$ for $\Sigma_{out} = 0.1$. This avoids the detection of false-positive peaks due to Poisson noise in the Σ_{bg} estimates, binary stars, or unresolved galaxies in *Gaia* that are expected to show more clustering than stars. Particularly for binary star systems or unresolved galaxies, the pairs of them are much more likely to occur because they are more correlated; thus they are likely to reach 5 significance and cause false positives.

Table 2. The nine known GCs and the two known galaxies found in our detection and their detected positions (α and δ), significance values (S), and inner kernel sizes (σ_1). Only Fornax 1–6 are actual clusters belonging to their parent dwarf galaxy.

Objects	α [°]	δ [°]	S	σ_1 [pc]
Fornax 1	40.5871	− 34.1016	8.5	10
Fornax 2	39.6842	− 34.8092	8.2	10
Fornax 3	39.9502	− 34.2593	7.4	10
Fornax 4	40.0343	− 34.5375	5.4	10
Fornax 5	39.2570	− 34.1845	7.5	10
Fornax 6	40.0298	− 34.4204	5.2	10
Palomar 3	151.3788	0.0731	7.3	10
Messier 75	301.5206	− 21.9233	37.6	10
NGC 5466	211.3615	28.5321	37.7	10
Leo I	152.1122	12.3001	37.2	10
Sextans A	151.3799	0.0714	6.3	10

After running the searching algorithm on all 55 targeted dwarfs, we identify 11 stellar overdensity candidates, based on the highest detected significance of each candidate if it is detected multiple times with different searching parameters. Cross-matched with the SIMBAD data base (Wenger et al. 2000), all 11 candidates are known objects. Nine of them are known GCs: Fornax GC 1–5 (Shapley 1938; Hodge 1961), Fornax GC 6 (Shapley 1939; Verner et al. 1981; Demers, Irwin & Kunkel 1994; Stetson, Hesser & Smecker-Hane 1998; Wang et al. 2019), Messier 75 (Shapley & Sawyer 1927), NGC 5466 (Shapley & Sawyer 1927), and Palomar 3 (Wilson 1955). The other two of them are known galaxies: the Leo I dwarf spheroidal galaxy (Harrington & Wilson 1950) and the Sextans A dwarf irregular galaxy (Zwicky 1942). We remark that Leo I is found when searching for overdensities near Segue I, as they are close to each other in the sky. Table 2 summarizes the 11 known objects and their detected positions (RA and Dec), significance values (S), and inner kernel sizes (σ_1). Fig. 3 shows the stellar distribution of *Gaia* sources for the six GCs of Fornax and the corresponding images from DES DR1 (Abbott et al. 2018) made with the HiPS (Hierarchical Progressive Surveys; Fernique et al. 2015). The yellow circles show the inner kernel of 10 pc (note that it happens to be that all the significance values with 10 pc are greater than with 3 or 5 pc in our detection of the nine GCs). Most of those known GCs are detected with the strong significance of $S > 7$ except for Fornax GC 6 with $S = 5.2$, which emphasizes that our algorithm can detect GCs from the regions of

[2] $\int_5^\infty \frac{1}{\sqrt{2\pi}} e^{-0.5z^2} dz \sim 10^{-7}$

[3] The searching radius of 8° corresponds to $\sim 10^4$ pc at the distance of 100 kpc so the searching area is $\sim 10^8$ pc^2. With the spatial resolution ~ 1 pc^2, the total number of pixels is then $\sim 10^8$.

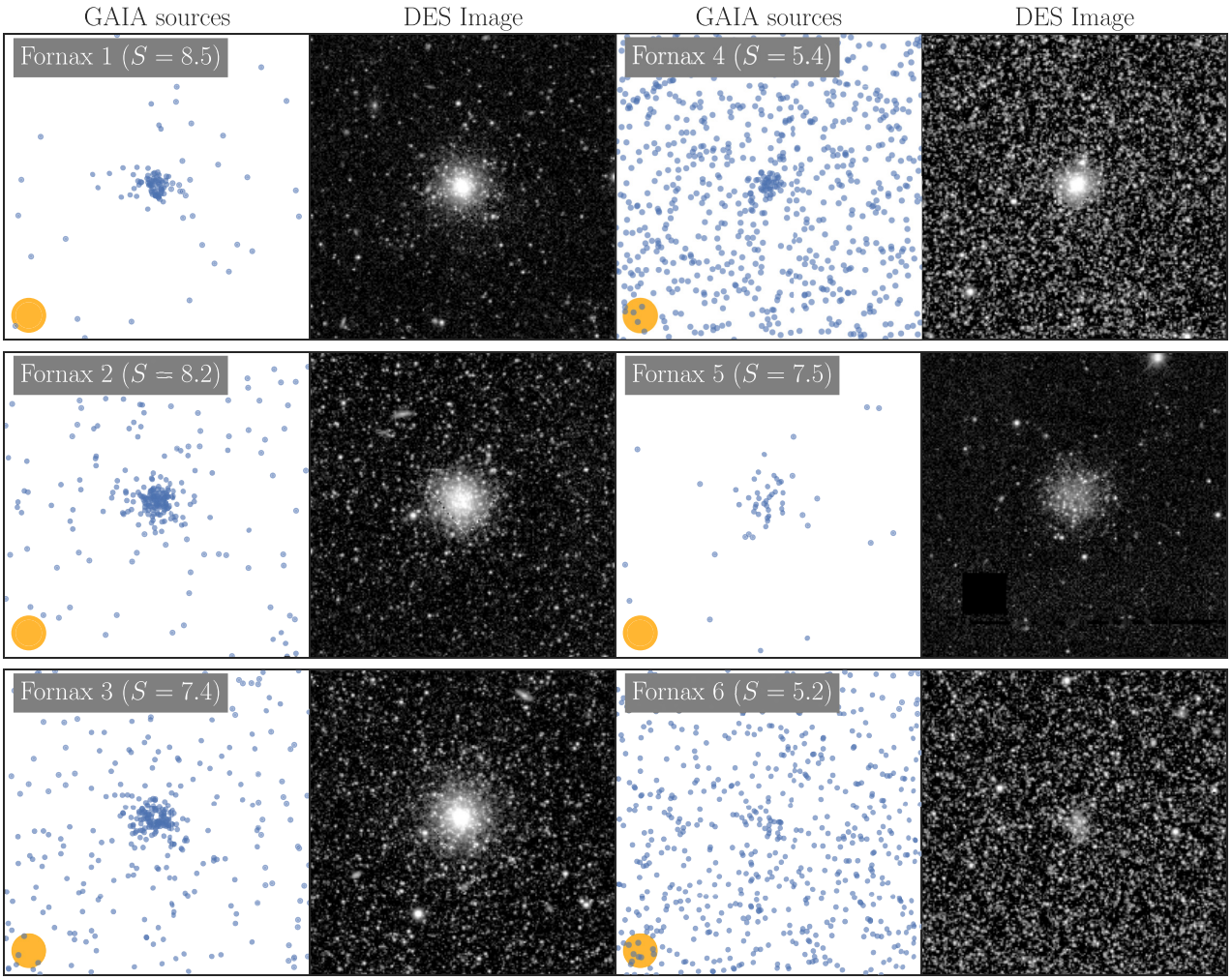

Figure 3. The source maps and the images of the six GCs of Fornax. *Left* and *Middle-right* panels: the stellar distributions of *Gaia* sources centred at each overdensity satisfying the detection criteria. The legends show the names of GCs and their significance values S. The yellow circles illustrate the inner kernel size of 10 pc. The dimension of each panel is 100×100 pc^2. *Middle-left* and *Right* panels: the corresponding images from DES DR1 made with the HIPS.

high stellar density such as Fornax GC 6. Fig. 3 further indicates that the significance values are reasonable: bright GCs located at low-density areas (e.g. Fornax GC 1 and 2) have high significance ($S > 8$) and faint GCs located at high-density areas (e.g. Fornax GC 6) have low significance ($S \sim 5$). However, we are aware of missing the ultra-faint GC in the Eridanus 2 in our detection, which we will further discuss later in Section 4.2.

4 DISCUSSION

4.1 Detection limit in *V*-band magnitude

In this section, we will demonstrate how we carry out the detection limit in V-band magnitude $M_{\rm V}^{\rm lim}$ of the search for each targeted dwarf, which indicates that GCs brighter than $M_{\rm V}^{\rm lim}$ are detectable in our search. To do so, we generate 1000 mock GCs with luminosity in the range of $-10 < M_{\rm V} < 0$ assuming the age =12 Gyr and [Fe/H] $= -2$ of the stellar populations. Sampling the stars of each GC population according to the lognormal initial mass function in Chabrier (2005), we interpolate the isochrone based on the PARSEC isochrone (Bressan et al. 2012), then utilizing the isochrones of all the mock GC stellar populations to carry out the detection limit for each targeted dwarf as follows.

Given a targeted dwarf, to compute the detection limit $M_{\rm V}^{\rm lim}$, we first calculate the number of observable stars of each mock GC satisfying the G-band selection by counting the number of stars within $17 < G < 21$ according to its isochrone at the distance of the dwarf. Based on the number of observable stars, we compute the number of stars of each GC within the inner kernel size σ_1 as

$$\Sigma_{\rm in}^{\rm obs} = f\,(\sigma_1;\, r_{\rm h} = 3{\rm pc}) \times ({\rm total\ number\ of\ observable\ stars})\,, \quad (9)$$

where $f\,(\sigma_1;\, r_{\rm h}) = \sigma_1^2/\sigma_1^2 + r_{\rm h}^2$ is the fraction of the number of stars within the radius of σ_1 according to the Plummer model of 2D surface density profile of a GC with a half-light radius $r_{\rm h} = 3$pc (Plummer 1911). With $\Sigma_{\rm in}^{\rm obs}$ of all the mock GCs at hand, we then use a linear best fit to describe the relation between $\log_{10}\left(\Sigma_{\rm in}^{\rm obs}\right)$ and $M_{\rm V}$ of the GCs. According to the maximum background estimate of the given dwarf, we know the threshold number of stars $\Sigma_{\rm in}^{\rm lim}$ to be observed to reach 5 significance. By comparing $\Sigma_{\rm in}^{\rm lim}$ to the best fit, we can obtain the detection limit $M_{\rm V}^{\rm lim}$ for the given targeted dwarf.

We take the Fornax dwarf as an example of the procedure of injection of mock GCs. In the left-hand panel of Fig. 4, we show

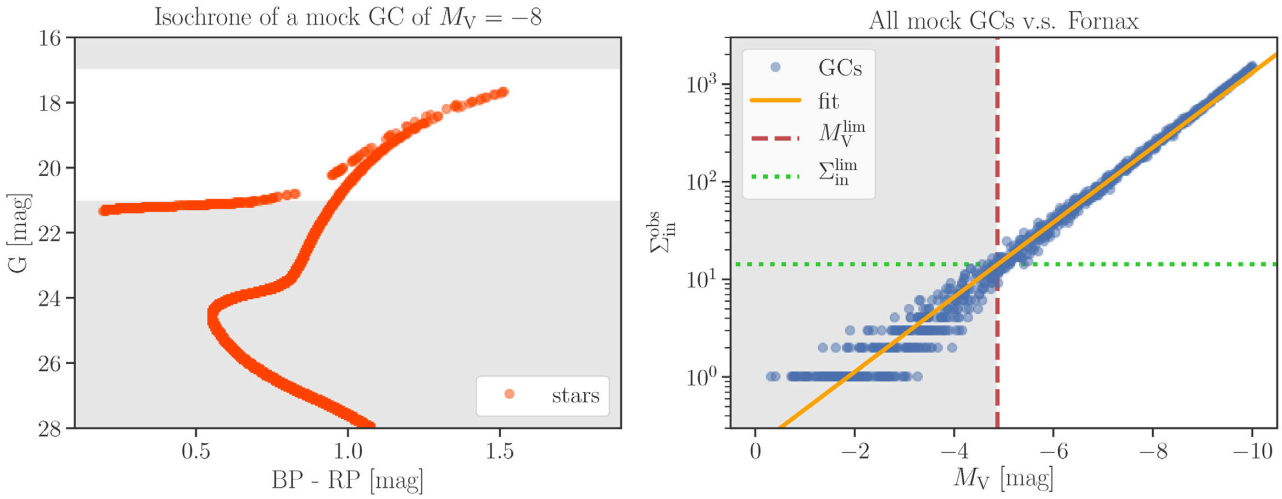

Figure 4. *Left*: the isochrone of a single mock GC of $M_V = -8$ at the distance of the Fornax dwarf spheroidal. The stars in the white area are observable within our *Gaia G*-band cut. *Right*: the numbers of observable stars Σ_{in}^{obs} versus M_V of all 1000 mock GCs for Fornax. The green dashed line shows the threshold number of stars Σ_{in}^{lim} to reach 5 significance according to the maximum background estimate of Fornax. The yellow line is the linear best fit and the red dashed line is the detection limit M_V^{lim} derived based on the best fit and Σ_{in}^{lim}. The GCs in the white area are detectable.

the isochrone of a single mock GC of $M_V = -8$ at the distance of Fornax and the stars in the white area are observable within our *Gaia G*-band cut. By counting the number of stars satisfying $17 < G < 21$ corrected by the fraction of stars located within the inner kernels, we know the number of observable stars Σ_{in}^{obs} for the given mock GC. Applying the calculation of Σ_{in}^{obs} for each mock GC, we show the relation between Σ_{in}^{obs} and M_V for all the mock GCs in the right-hand panel of Fig. 4. The green dashed line shows the threshold number of stars Σ_{in}^{lim} to reach $S = 5$ according to the maximum background estimate of Fornax; that is, the GCs above the green dashed line are expected to be detectable. Fitting the relation between $\log_{10}\left(\Sigma_{in}^{obs}\right)$ and M_V with a linear best fit as shown in the yellow line, we solve the detection limit M_V^{lim} by finding the value of M_V satisfying the fit at the value of Σ_{in}^{lim} (the green dashed line). The red dashed line indicates the derived M_V^{lim} and the GCs brighter than M_V^{lim} in the white area are thus detectable in our search. It is worth noting that the *Gaia* magnitude limit is brighter than $G = 21$ in some areas of the sky, which will decrease Σ_{in}^{obs} if it happens in our targeted area, resulting in a brighter M_V^{lim}.

Repeating the same calculation of M_V^{lim} for all the targeted dwarfs, we obtain the detection limits of the dwarfs and show the comparison of the derived M_V^{lim} to the distances and the luminosities of the dwarfs in Fig. 5. In the left-hand panel, there is an obvious trend that the M_V^{lim} are fainter for the dwarfs that are closer because the injected Σ_{in}^{obs} of the GCs for these dwarfs with small distance modulus is typically larger than that of the dwarfs with large distance modulus. On the other hand in the right-hand panel, the relation between M_V^{lim} and M_V of the dwarfs is more scattered yet there is a slight trend of fainter M_V^{lim} for the fainter dwarfs. This is likely because the faint dwarfs, compared to the bright ones, tend to have less-crowded stellar distributions and hence lower thresholds Σ_{in}^{lim} to reach 5 significance. To sum up, the faint M_V^{lim} for the close dwarfs or the faint dwarfs is reasonable because the ability of dwarfs to hide GCs from our detection is intuitively weaker for the dwarfs that are closer or fainter. It is also worth noting that most of the time M_V^{lim} with $\sigma_1 = 10$ pc is the faintest, M_V^{lim} with $\sigma_1 = 5$ pc is the intermediate, and M_V^{lim} with $\sigma_1 = 3$ pc is the brightest mainly because the fractions of stars observed within the inner kernels are around 0.9, 0.7, and 0.5 for $\sigma_1 = 10$, 5, and 3 pc, respectively according to the Plummer model. That is, the low Σ_{in}^{obs} due to the small fraction for small σ_1 makes the faint GCs less likely to meet 5 significance, thus resulting in a bright M_V^{lim}.

4.2 Completeness of the search

With the limiting magnitudes of GC detection at hand, we can calculate the completeness of the search according to the typical GC luminosity function (GCLF). In this section, we will calculate the completeness factor g with three different GCLFs: (a) the typical MW GCLF in Harris (2001): a Gaussian distribution with a peak at $M_V = -7.4$ and a standard deviation of 1.2, $\mathcal{N}(-7.4,\ 1.2^2)$, (b) the evolved Schechter function in Jordán et al. (2007) with a peak at $M_V \sim -7.4$, and (c) a presumed Gaussian distribution with a peak at $M_V = -6$ and a standard deviation of 1.2, $\mathcal{N}(-6,\ 1.2^2)$. We calculate g by evaluating the cumulative distribution functions of those GCLFs at M_V^{lim} based on the search with $\sigma_1 = 10$ pc thanks to its better detecting sensitivity compared to $\sigma_1 = 3$ and 5 pc (all the detected objects with the highest significance are detected with $\sigma_1 = 10$ pc in Section 3).

We begin with the GCLF in (a); in the MW, the GCLF is approximately a Gaussian distribution of $\mathcal{N}(-7.4,\ 1.2^2)$ (Harris 2001). With this MW GCLF, we compute the completeness factor g and show them in the blue points in Fig. 6. The completeness of the search is higher than 90 per cent for most of the dwarfs and around 70 per cent for the lowest three, Eridanus 2, Leo T, and Phoenix. This high completeness is a consequence of $M_V^{lim} > -7$ for all the dwarfs; that is, the detection limits are fainter than the peak magnitude of the MW GCLF. Besides, as a result of the trend of brighter M_V^{lim} for the farther targeted dwarfs in the left-hand panel of Fig. 5, the completeness gets lower for the dwarfs that are more distant. In addition, Villegas et al. (2010) described that the dispersion of GCLF can be as small as 0.5 for small dwarfs. Calculating the completeness with this GCLF, we find that the result is almost the same as that of the MW GCLF.

Compared to the Gaussian MW GCLF peaking at $M_V = -7.4$, the evolved Schechter function with a similar peak magnitude proposed in Jordán et al. (2007) can describe the GCLF well too, particularly

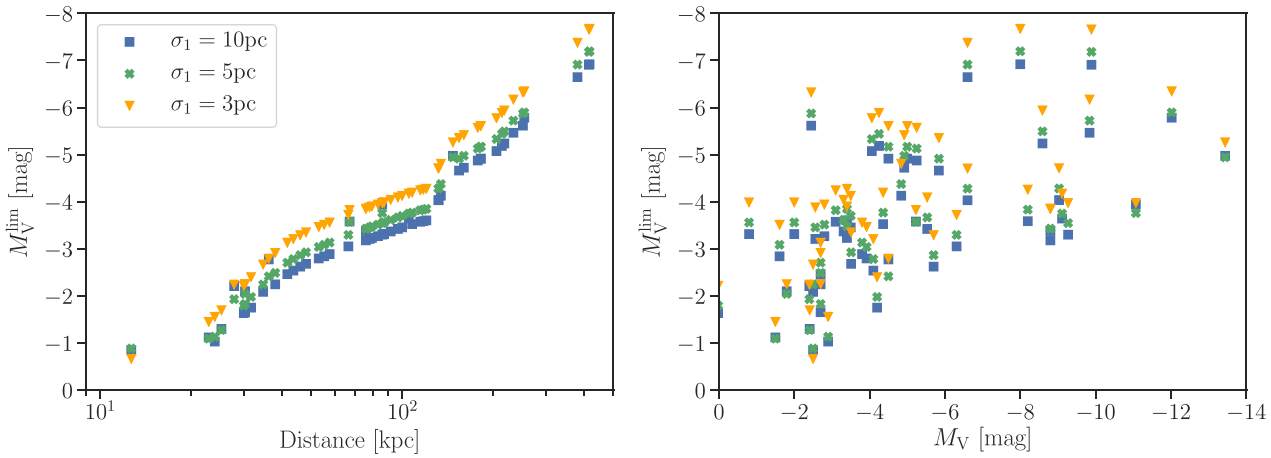

Figure 5. The detection limit M_V^{lim} of all targeted dwarfs with the different inner kernels $\sigma_1 = 3$, 5, and 10 pc. *Left*: M_V^{lim} versus the distance of the dwarfs. *Right*: M_V^{lim} versus the M_V of the dwarfs.

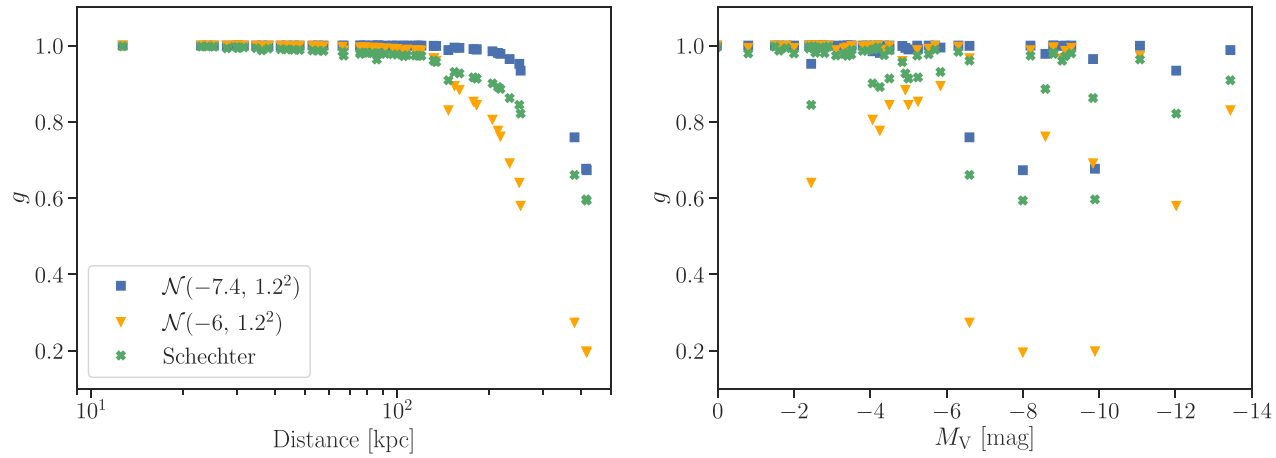

Figure 6. The completeness g of the GC search for all targeted dwarfs with three GCLFs: the Gaussian of $\mathcal{N}(-7.4,\ 1.2^2)$ and $\mathcal{N}(-6,\ 1.2^2)$ and the evolved Schechter in Jordán et al. (2007). *Left*: Completeness versus the distance of the dwarfs. *Right*: Completeness versus dwarf galaxy luminosity.

taking good care of the low-mass faint GCs. We compute the completeness factor g with this GCLF as shown in the green points in Fig. 6, finding that the difference in g with this GCLF from the traditional Gaussian is less than 5–10 per cent lower. The reason for the larger difference (∼10 per cent) in g of the two GCLFs for the targeted dwarfs that are more distant than 100 kpc is that the probability density of the evolved Schechter function is higher than that of the Gaussian MW GCLF in the faint end. Thus as these dwarfs have brighter M_V^{lim} than the close dwarfs, their cumulative distribution functions at M_V^{lim} of the evolved Schechter GCLF are lower than that of the Gaussian MW GCLF. On the other hand, for the dwarfs that are closer than 100 kpc, M_V^{lim} is much fainter than the peaks of the two GCLFs so the corresponding g approaches 1 for both GCLFs.

So far, we have assumed the GC population for all the dwarfs follows the GCLFs based on the results from bright galaxies, the Gaussian in Harris (2001) and the evolved Schechter in Jordán et al. (2007). These two GCLFs have similar peaks but different shapes: the evolved Schechter one extends more towards the faint end to account for faint GCs (see the black curves in Fig. A1). However, these GCLFs might not hold in the faint host galaxies such as the faint satellites of the MW since there has been no reason for them being universal. Especially some of the dwarfs investigated in the paper are even fainter than the peak magnitude of these GCLFs, whether such systems may host GCs that are brighter than the dwarfs themselves is unclear, and is probably unlikely. Despite the lack of robust constraints on this, van den Bergh (2006) has pointed out that the peak of GCLF can be at $M_V = -5$ for faint galaxies. Moreover, the peak magnitude of GCLFs for different galaxies can vary in the range of $-7 < M_V < -5$ (see Richtler 2003, Table 2 in particular). Therefore, we look at the known GC populations of the MW, NGC 6822, Sagittarius, Fornax, and Eridanus 2 in Appendix A and decide to consider the peak of GCLF at $M_V = -6$ based on Fig. A1 to calculate the completeness again. The orange points in Fig. 6 show the completeness g computed with the GCLF $\mathcal{N}(-6,\ 1.2^2)$. As this GCLF peaks at the fainter magnitude than the other two GCLFs, g hardly changes for close dwarfs with much fainter M_V^{lim} than the peak of GCLF at $M_V = -6$ whereas g drops for the ones that are more distant than 100 kpc with small M_V^{lim}, e.g. $g = 20$–30 per cent for Eridanus 2, Leo T, and Phoenix.

Section 3 has mentioned that the ultra-faint GC with the luminosity of $M_V = -3.5$ (Koposov et al. 2015; Crnojević et al. 2016) in the Eridanus 2 is missing in our detection. This is mainly because the

luminosity of this GC is much fainter than the detection limit $M_V^{\rm lim} \sim -6.5$ for the Eridanus 2 in the search. Hosting the ultra-faint GC of $M_V = -3.5$ and having the luminosity of $M_V = -6.6$ close to the peak magnitude of the MW GCLF, the Eridanus 2 is likely to have a GCLF peaking at a fainter magnitude than $M_V = -7.4$. As shown in Fig. 6, the completeness g for the Eridanus 2 is 75 per cent with the Gaussian MW GCLF and 65 per cent with the evolved Schechter GCLF. When we shift the peak of GCLF to $M_V = -6$, the completeness factor drops to only 30 per cent for the Eridanus 2, which further explains the existence of the ultra-faint GC in the Eridanus 2 while it is missing in our search.

4.3 Specific frequency of the globular clusters

The specific frequency of GCs is a common quantity to indicate the richness of GC system for a galaxy, first formulated as $S_N = N_{gc} \times 10^{0.4(M_{V,gal}+15)}$ where N_{gc} is the total number of GCs in a host galaxy and $M_{V,gal}$ is the absolute magnitude of the host galaxy (Harris & van den Bergh 1981). With $L_{gal} \equiv 10^{-0.4(M_{V,gal}+15)}$ defined as the galactic V-band luminosity normalized to $M_V = -15$, $S_N = N_{gc}/L_{gal}$ then indicates the number of GCs per unit normalized luminosity. When the galaxy luminosity and the number of clusters are large, simply taking a ratio between the number and luminosity makes sense; however, a more statistical approach is required for dwarf galaxies.

Here, we define S_N as the specific frequency for a group of galaxies. In that case, the observed number of clusters for each galaxy in a group will be Poisson distributed:

$$N_{gc} \sim \text{Poisson}\left(S_N L_{gal}\right) \tag{10}$$

where L_{gal} is the luminosity of the galaxy and N_{gc} is the random variable describing the number of clusters in this galaxy. Assuming that our samples of GCs are incomplete with different completeness correction g for each dwarf, we can update the model to include incompleteness as

$$N_{gc} \sim \text{Poisson}\left(S_N g L_{gal}\right). \tag{11}$$

Among the nine objects that we identify in our search in Section 3, only the six GCs found around the Fornax dwarf are associated with the parent dwarf galaxy. That is, the dwarfs targeted in the paper except for Fornax have no associated GCs detected around them. Due to the lack of associated GCs and the fact that most of the dwarfs are much fainter than Fornax, the formal S_N is hence expected to be zero with large upper bounds. To properly take into account the non-detections and to still be able to constrain the specific frequency of the dwarf population, we assume that S_N is constant for the dwarfs with similar luminosities and will provide upper bounds on S_N for the dwarf population as a whole.

Assuming that we look at m dwarfs as a group at once, we know the luminosity L_i and the completeness g_i for the $i^{\rm th}$ dwarf, where $1 \leq i \leq m$. The total expected number of observed GCs in this group of m dwarfs is the sum of the expected number of GCs in each dwarf. Defining $L \equiv \sum_{i=1}^{m} L_i g_i$ and with the constant specific frequency S_N shared among the m dwarfs, we can write down the total expected number of GCs as

$$\sum_{i=1}^{m} S_N g_i L_i = S_N \sum_{i=1}^{m} g_i L_i \equiv S_N L. \tag{12}$$

Together with the definition of the total number of observed GCs of the m dwarfs as $N = \sum_{i=1}^{m} N_i$ where N_i is the number of observed GCs of the $i^{\rm th}$ dwarf from our detection. We model N similarly to equation (11) as $N \sim \text{Poisson}(S_N L)$ and therefore the likelihood function $P(N \mid S_N) \propto S_N^N e^{-S_N L}$. Using the Jeffreys prior $S_N^{-1/2}$ as the distribution of the parameter S_N, we have the posterior distribution

$$P(S_N \mid N) \propto P(S_N) P(N \mid S_N) \propto S_N^{N-\frac{1}{2}} e^{-S_N L}. \tag{13}$$

This is a Gamma distribution; that is, $S_N \sim \text{Gamma}\left(N + \frac{1}{2}, L\right)$.

With the posterior in equation (13), we construct the 90 per cent credible intervals on the parameter S_N with the Gaussian MW GCLF for the dwarfs as shown in the blue curve in the left-hand panel of Fig. 7. Also, we show the S_N of the MW and its four most luminous satellites (LMC, SMC, Sagittarius, and Fornax) based on Forbes et al. (2000) and the mean trend curve of S_N of 100 galaxies in the Virgo Cluster from Peng et al. (2008). Separating the Fornax dwarf from the others due to its richness of GCs, we first calculate its double-sided credible interval on the specific frequency of $12 < S_N < 47$. For the other dwarfs with no discovered GCs, we bin the ones brighter than $M_V = -7$ with a window width of 2 mag and look at the others all at once, where the value of $M_V = -7$ is chosen as it is close to the peak magnitude of the GCLF. For the dwarfs in each bin, we obtain the one-sided credible intervals as the upper bounds of the specific frequency: $S_N < 20$ for the dwarfs with $-12 < M_V < -10$, $S_N < 30$ for the dwarfs with $-10 < M_V < -7$, and $S_N < 90$ for the dwarfs with $M_V > -7$. Similarly, we also construct the credible intervals on S_N with the evolved Schechter GCLF for the dwarfs, finding a similar result as with the Gaussian MW GCLF. The difference in S_N with the two GCLFs is less than 5–10 per cent so we only show the one with $\mathcal{N}(-7.4,\ 1.2^2)$ in Fig. 7.

The reason for grouping the dwarfs fainter than $M_V = -7$ is that they are in general faint so the expected number of GCs is much smaller than one, which makes them not very informative. Besides, the posterior becomes more prior-dependent for the fainter dwarfs as well. Thus, finding no GCs for the dwarfs in the brighter M_V bins constrains the upper bounds stronger than in the fainter bins. Especially at $M_V < -10$, the relatively low upper bounds indicate that the Fornax dwarf has a relatively higher S_N than the other dwarfs, especially than the ones with $M_V < -10$.

As mentioned in Section 4.2, the completeness will drop if the GCLF peaks at a fainter M_V than the typical peak magnitude at $M_V = -7.4$, which would effectively increase the upper bounds on S_N because the dropping completeness decreases the L. We therefore calculate the credible intervals on S_N again for the dwarfs with the GCLF $\mathcal{N}(-6,\ 1.2^2)$ as the orange curve shows in the left-hand panel of Fig. 7, finding that the upper bounds on S_N with this shifted GCLF (the orange curve) are higher than that with the MW GCLF (the blue curve) as expected. This effect is also expected to influence the upper limits more for the fainter dwarfs since the GCLFs are expected to shift more if the host galaxies are fainter; however, the upper limit is already more prior-dependent and less informative on the faint end so this upper limit increasing effect is less influential.

Besides S_N, the probability of a galaxy with luminosity L and S_N to host N GCs, $P(N; S_N L)$, is also interesting. With the 90 per cent credible intervals on S_N, we show the range of $P(N = 0; S_N L)$ for a galaxy with L based on the model $N \sim \text{Poisson}(S_N L)$ in the right-hand panel of Fig. 7, which indicates the probability of a galaxy to host no GCs. Except for Fornax, the upper limits of S_N result in the lower limits of $P(N = 0; S_N L)$. Based on $P(N = 0; S_N L)$, galaxies fainter than $M_V = -9$ have $P(N = 0; S_N L) > 0.9$, which means the probability of these galaxies to have at least one GC is lower than 10 per cent. Our finding of $P(N = 0; S_N L) > 0.9$ for galaxies with $M_V > -9$ is in agreement with the claims of the lowest galaxy mass of $\sim 10^5\,M_\odot$ or luminosity $M_V \sim -9$ to host at least one GC from

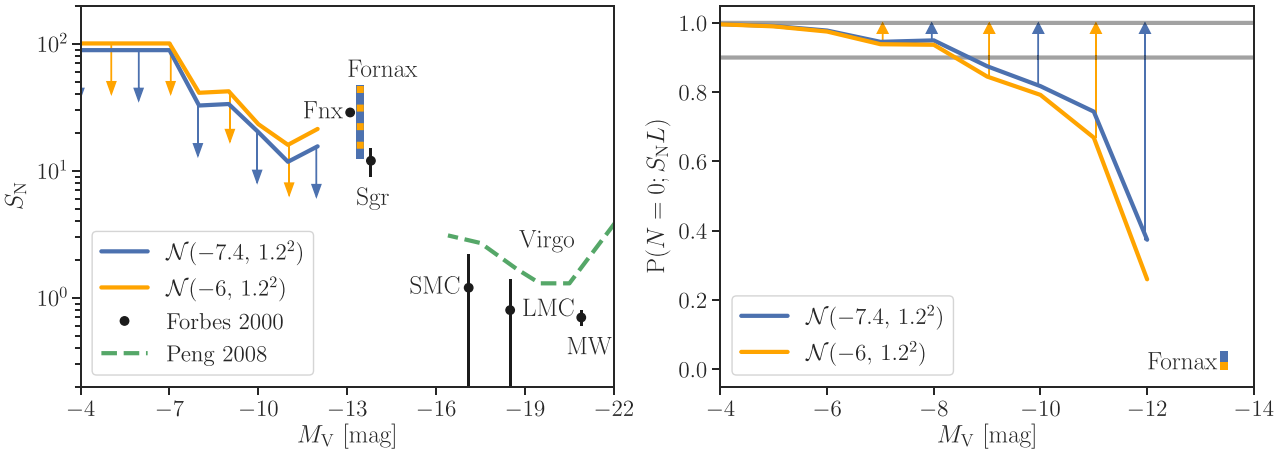

Figure 7. *Left*: The 90 per cent credible intervals on S_N versus M_V of the dwarfs with two different GCLFs: double-sided intervals for Fornax and one-sided upper bounds for the others. The black data points are S_N of the MW, LMC, SMC, Sagittarius (Sgr), and Fornax (Fnx) in Forbes et al. (2000). The green dashed curve is the mean trend curve of the S_N for 100 galaxies in the Virgo Cluster in Peng et al. (2008). *Right*: The probability of hosting no GC for a galaxy with luminosity L and specific frequency S_N, $P(N = 0; S_N L)$. The 90 per cent credible intervals on S_N is used to derive the range of $P(N = 0; S_N L)$. The two greys lines indicate $P(N = 0; S_N L) = 0.9$ and $P(N = 0; S_N L) = 1$.

Georgiev et al. (2010) and Forbes et al. (2018). This may further explain the observation that galaxies less massive than 10^6 $M_\odot$ tend not to have nuclei (Sánchez-Janssen et al. 2019) if we assume that the nuclei originate from GCs sunk by dynamical friction to the centre. Given our constraints on the specific frequency, Eridanus 2 with $M_V \sim -7$ has $P(N = 0; S_N L) \sim 0.95$, which highlights that the GC inside Eridanus 2 is indeed an outlier.

5 CONCLUSIONS

We have reported the results of the search for possibly hiding GCs around 55 dwarf galaxies within the distance of 450 kpc from the Galactic Centre excluding the LMC, SMC, and Sagittarius. This was a targeted search around the dwarfs so we excluded those three satellites to avoid a huge portion of the sky to be searched due to their relatively large sizes. For each targeted dwarf galaxy, we have investigated the stellar distribution of the sources in *Gaia* DR2, selected with the magnitude, proper motion, and stellar morphology cuts.

Using the kernel density estimation and the Poisson statistics of stellar number counts, we have identified 11 stellar density peaks of above 5 significance as possible GC candidates in the targeted area. Cross-matching the 11 possible candidates with the SIMBAD data base and existing imaging data, we have found that all of them are known objects: Fornax GC 1–6, Messier 75, NGC 5466, Palomar 3, Leo I, and Sextans A. Only the six GCs of Fornax are associated with the parent dwarf galaxy.

We have calculated the GC detection limit in M_V for each dwarf using 1000 simulated GCs, finding that $M_V^{\rm lim} > -7$ for all the dwarfs. According to the $M_V^{\rm lim}$ of the dwarfs, we have then calculated the completeness of detection with the Gaussian MW GCLF $\mathcal{N}(-7.4, 1.2^2)$, the evolved Schechter GCLF peaking at $M_V^{\rm lim} \sim -7.4$, and the assumed Gaussian GCLF $\mathcal{N}(-6, 1.2^2)$. With the Gaussian MW GCLF and the evolved Schechter GCLF, the completeness of the detection for most of the dwarfs was higher than 90 per cent and even that of the lowest three, Eridanus 2, Leo T, and Phoenix, was around 70 per cent. With the assumed Gaussian GCLF, the completeness of our search was lower for the dwarfs that are more distant than 100 kpc, such as the Eridanus 2, Leo T, and Phoenix where it reached 20–30 per cent. Using the completeness, we have constructed the 90 per cent credible intervals on the GC specific frequency S_N of the MW dwarf galaxies. The Fornax dwarf had the credible interval on the specific frequency of $12 < s < 47$, the dwarfs with $-12 < M_V < -10$ had $S_N < 20$, the dwarfs with $-10 < M_V < -7$ had $S_N < 30$, and dwarfs with $M_V > -7$ had non-informative $S_N < 90$. Based on these credible intervals on S_N, we have derived the probability of galaxies to host GCs given their luminosity, finding that the probability of galaxies fainter than $M_V = -9$ to possess GCs is lower than 10 per cent.

ACKNOWLEDGEMENTS

We acknowledge the support by NSF grants AST-1813881, AST-1909584, and Heising-Simons Foundation grant 2018-1030. This paper has made use of the Whole Sky Database (wsdb) created by Sergey Koposov and maintained at the Institute of Astronomy, Cambridge with financial support from the Science & Technology Facilities Council (STFC) and the European Research Council (ERC). This software has made use of the Q3C software (Koposov & Bartunov 2006).

This work presents results from the European Space Agency (ESA) space mission *Gaia*. *Gaia* data are being processed by the *Gaia* Data Processing and Analysis Consortium (DPAC). Funding for the DPAC is provided by national institutions, in particular the institutions participating in the *Gaia* MultiLateral Agreement (MLA). The *Gaia* mission website is https://www.cosmos.esa.int/gaia. The *Gaia* archive website is https://archives.esac.esa.int/gaia.

Software: NUMPY (van der Walt et al. 2011), SCIPY (Jones et al. 2001), PANDAS (Mckinney 2010), MATPLOTLIB (Hunter 2007), SEABORN (Waskom et al. 2016), ASTROPY (Astropy Collaboration 2013), IMF (Ginsburg et al. 2020), and SQLUTILPY (Koposov 2018).

DATA AVAILABILITY

The data underlying this article were derived from sources in the public domain: https://archives.esac.esa.int/gaia.

REFERENCES

Abbott T. M. C. et al., 2018, ApJS, 239, 18
Arenou F. et al., 2018, A&A, 616, A17
Astropy Collaboration, 2013, A&A, 558, A33
Beasley M. A., Trujillo I., Leaman R., Montes M., 2018, Nature, 555, 483
Bellazzini M., Ferraro F. R., Ibata R., 2003, AJ, 125, 188
Boylan-Kolchin M., 2018, MNRAS, 479, 332
Bressan A., Marigo P., Girardi L., Salasnich B., Dal Cero C., Rubele S., Nanni A., 2012, MNRAS, 427, 127
Brodie J. P., Strader J., 2006, ARA&A, 44, 193
Chabrier G., 2005, in Corbelli E., Palla F., Zinnecker H., eds, Astrophysics and Space Science Library, Vol. 327, The Initial Mass Function 50 Years Later. Springer, Dordrecht, p. 41
Choksi N., Gnedin O. Y., 2019, MNRAS, 486, 331
Crnojević D., Sand D. J., Zaritsky D., Spekkens K., Willman B., Hargis J. R., 2016, ApJ, 824, L14
Demers S., Irwin M. J., Kunkel W. E., 1994, AJ, 108, 1648
Drlica-Wagner A. et al., 2015, ApJ, 813, 109
El-Badry K., Quataert E., Weisz D. R., Choksi N., Boylan-Kolchin M., 2019, MNRAS, 482, 4528
ESA DPAC, 2019, Documentation release 1.2, https://gea.esac.esa.int/archive/documentation/GDR2/Gaia_archive/chap_datamodel/sec_dm_main_tables/ssec_dm_gaia_source.html
Fernique P. et al., 2015, A&A, 578, A114
Forbes D. A., Brodie J. P., Grillmair C. J., 1997, AJ, 113, 1652
Forbes D. A., Masters K. L., Minniti D., Barmby P., 2000, A&A, 358, 471
Forbes D. A., Read J. I., Gieles M., Collins M. L. M., 2018, MNRAS, 481, 5592
Fritz T. K., Battaglia G., Pawlowski M. S., Kallivayalil N., van der Marel R., Sohn S. T., Brook C., Besla G., 2018, A&A, 619, A103
Gaia Collaboration, 2016, A&A, 595, A1
Gaia Collaboration, 2018a, A&A, 616, A1
Gaia Collaboration, 2018b, A&A, 616, A12
Georgiev I. Y., Puzia T. H., Goudfrooij P., Hilker M., 2010, MNRAS, 406, 1967
Ginsburg A., Koposov S., Christian T., 2020, Imf: Simple Tools to Work with the Initial Mass Function.
Gratton R., Sneden C., Carretta E., 2004, ARA&A, 42, 385
Gratton R., Bragaglia A., Carretta E., D'Orazi V., Lucatello S., Sollima A., 2019, A&AR, 27, 8
Hargis J. R. et al., 2016, ApJ, 818, 39
Harrington R. G., Wilson A. G., 1950, PASP, 62, 118
Harris W. E., 1991, ARA&A, 29, 543
Harris W. E., 1996, AJ, 112, 1487
Harris W. E., 2001, in Labhardt L., Binggeli B., eds, Saas-Fee Advanced Course 28: Star Clusters. Springer-Verlag, Berlin, p. 223
Harris W. E., 2010, preprint (arXiv:1012.3224)
Harris W. E., van den Bergh S., 1981, AJ, 86, 1627
Harris G. L. H., Harris W. E., Poole G. B., 1999, AJ, 117, 855
He C.-C., Ricotti M., Geen S., 2020, MNRAS, 492, 4858
Hodge P. W., 1961, AJ, 66, 83
Homma D. et al., 2016, ApJ, 832, 21
Homma D. et al., 2018, PASJ, 70, S18
Howard C. S., Pudritz R. E., Harris W. E., 2018a, Nat. Astron., 2, 725
Howard C. S., Pudritz R. E., Harris W. E., Klessen R. S., 2018b, MNRAS, 475, 3121
Hunter J. D., 2007, Comput. Sci. Eng., 9, 90
Jones E. et al., 2001, SciPy: Open Source Scientific Tools for Python, http://www.scipy.org/
Jordán A. et al., 2007, ApJS, 171, 101
Koposov S., 2018, Sqlutilpy Module to Access SQL Databases, https://github.com/segasai/sqlutilpy
Koposov S., Bartunov O., 2006, in Gabriel C., Arviset C., Ponz D., Enrique S., eds, ASP Conf. Ser. Vol. 351, Astronomical Data Analysis Software and Systems XV. Astron. Soc. Pac., San Francisco, p. 735
Koposov S. E., Glushkova E. V., Zolotukhin I. Y., 2008a, A&A, 486, 771
Koposov S. et al., 2008b, ApJ, 686, 279
Koposov S. E., Belokurov V., Torrealba G., Evans N. W., 2015, ApJ, 805, 130
Koposov S. E., Belokurov V., Torrealba G., 2017, MNRAS, 470, 2702
Kruijssen J. M. D., Pfeffer J. L., Reina-Campos M., Crain R. A., Bastian N., 2019, MNRAS, 486, 3180
Luque E. et al., 2017, MNRAS, 468, 97
Lynden-Bell D., Lynden-Bell R. M., 1995, MNRAS, 275, 429
Ma X. et al., 2020, MNRAS, 493, 4315
Mackey A. D., Gilmore G. F., 2003a, MNRAS, 338, 85
Mackey A. D., Gilmore G. F., 2003b, MNRAS, 338, 120
Mackey A. D., Gilmore G. F., 2003c, MNRAS, 340, 175
Mackey A. D., Gilmore G. F., 2004, MNRAS, 355, 504
McConnachie A. W., 2012, AJ, 144, 4
Mckinney W., 2010, Data Structures for Statistical Computing in Python, Proceedings of the 9th Python in Science Conference, p. 56
McLaughlin D. E., van der Marel R. P., 2005, ApJS, 161, 304
Massari D., Helmi A., 2018, A&A, 620, A155
Pace A. B., Li T. S., 2019, ApJ, 875, 77
Peng E. W. et al., 2008, ApJ, 681, 197
Plummer H. C., 1911, MNRAS, 71, 460
Reina-Campos M., Kruijssen J. M. D., Pfeffer J. L., Bastian N., Crain R. A., 2019, MNRAS, 486, 5838
Richtler T., 2003, in Alloin D., Gieren W., eds, Lecture Notes in Physics, Vol. 635, Stellar Candles for the Extragalactic Distance Scale. Springer-Verlag, p. 281
Sánchez-Janssen R. et al., 2019, ApJ, 878, 18
Searle L., Zinn R., 1978, ApJ, 225, 357
Shapley H., 1938, Nature, 142, 715
Shapley H., 1939, Proc. Natl. Acad. Sci. USA, 25, 565
Shapley H., Sawyer H. B., 1927, Harv. Coll. Obs. Bull., 849, 11
Simon J. D., 2018, ApJ, 863, 89
Stetson P. B., Hesser J. E., Smecker-Hane T. A., 1998, PASP, 110, 533
Torrealba G., Koposov S. E., Belokurov V., Irwin M., 2016a, MNRAS, 459, 2370
Torrealba G. et al., 2016b, MNRAS, 463, 712
Torrealba G. et al., 2018, MNRAS, 475, 5085
Torrealba G., Belokurov V., Koposov S. E., 2019a, MNRAS, 484, 2181
Torrealba G. et al., 2019b, MNRAS, 488, 2743
van den Bergh S., 2006, AJ, 131, 304
VandenBerg D. A., Brogaard K., Leaman R., Casagrand e L., 2013, ApJ, 775, 134
van der Walt S., Colbert S. C., Varoquaux G., 2011, Comput. Sci. Eng., 13, 22
Vasiliev E., 2019, MNRAS, 484, 2832
Veljanoski J. et al., 2015, MNRAS, 452, 320
Verner G., Demers S., Hardy E., Kunkel W. E., 1981, AJ, 86, 357
Villegas D. et al., 2010, ApJ, 717, 603
Walker M. G., Mateo M., Olszewski E. W., Gnedin O. Y., Wang X., Sen B., Woodroofe M., 2007, ApJ, 667, L53
Walsh S. M., Willman B., Jerjen H., 2009, AJ, 137, 450
Wang M. Y. et al., 2019, ApJ, 875, L13
Waskom M. et al. , 2016, seaborn: v0.7.0 , http://dx.doi.org/10.5281/zenodo.45133
Wenger M. et al., 2000, A&AS, 143, 9
Wilson A. G., 1955, PASP, 67, 27
Zwicky F., 1942, Phys. Rev., 61, 489

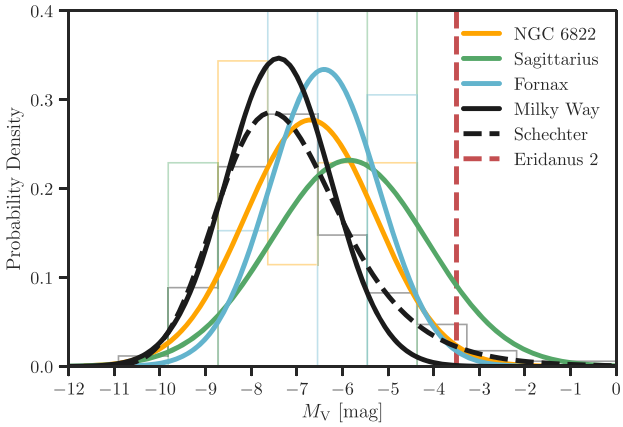

Figure A1. GCLFs of the MW, NGC 6822, Sagittarius, and Fornax. For each galaxy, the solid curve is the Gaussian fit to the histogram of the probability density of the number of GCs in each magnitude bin. The black dashed curve is the evolved Schechter function in Jordán et al. (2007). The red dashed line indicates the ultra-faint GC of the Eridanus 2.

APPENDIX A: GC LUMINOSITY FUNCTIONS

In Section 4, we adopt the Gaussian MW GCLF in Harris (2001) and the evolved Schechter GCLF in Jordán et al. (2007) for all the dwarfs to carry out the completeness factor and the specific frequency. However, the GCLF may shift towards the faint end for faint dwarfs, e.g. Richtler (2003) and van den Bergh (2006). To investigate this, we show the GCLFs in the histogram with Gaussian probability density distributions of the MW ($M_V \sim -21$), NGC 6822 ($M_V \sim -16$), Sagittarius ($M_V \sim -14$), and Fornax ($M_V \sim -13$) with the solid curves in Fig. A1. Besides, we also show the evolved Schechter GCLF with the black dashed curve and the ultra-faint GC of the Eridanus 2 ($M_V \sim -7$) with the red dashed line. We collect the GC lists for these galaxies according to Harris (2010), Veljanoski et al. (2015), Koposov et al. (2015), Vasiliev (2019), or the SIMBAD database. Based on the Gaussian distributions of the GCLFs and the existence of Eridanus 2 GC, there is a possible shift of the GCLF peak towards the faint luminosity for faint galaxies, e.g. the peaks of the dwarf galaxies are closer to $M_V \sim -6$ as opposed to the peak of the GC distribution in the MW at $M_V = -7.4$.

This paper has been typeset from a TEX/LATEX file prepared by the author.